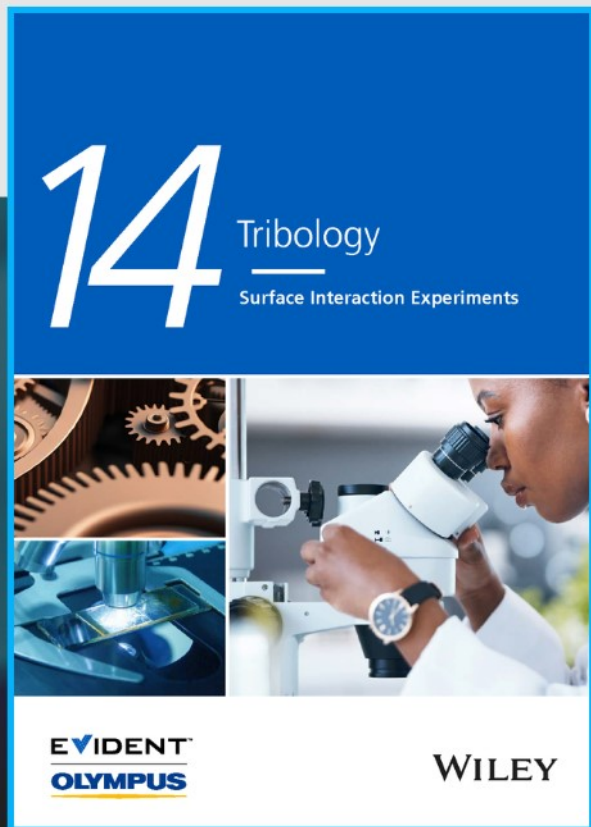




# Tribology: Surface Interaction Experiments



**The latest eBook from  
Advanced Optical Metrology.  
Download for free.**

Tribology has been a critical part of human civilization since ancient times, and it continues to play a crucial role in modern industries. Evident's eBook, in collaboration with Wiley, covers a broad range of topics, including the wear, friction, and lubrication of surfaces, testing methods, and the latest research on tribological phenomena at the nanoscopic level.

Don't miss out on the opportunity to dive into the world of tribology and gain a better understanding of the interaction of moving surfaces. Download our eBook now and stay ahead in the field of tribology.

**EVIDENT™**  
**OLYMPUS**

**WILEY**

## RESEARCH ARTICLE

POLYMER  
ENGINEERING  
AND SCIENCE

WILEY

# Synthesis of SnO<sub>2</sub>/TiO<sub>2</sub> micro belt fibers from polymer composite precursors and their applications in Li-ion batteries\*

Gabriel Gonzalez<sup>1</sup> | Md Toukir Hasan<sup>1</sup> | Daniel Ramirez<sup>2</sup> | Jason Parsons<sup>2</sup> | Mataz Alcoutlabi<sup>1</sup>

<sup>1</sup>Department of Mechanical Engineering,  
University of Texas, Edinburg, Texas, USA

<sup>2</sup>Department of Chemistry, University of  
Texas, Brownsville, Texas, USA

## Correspondence

Mataz Alcoutlabi, Department of  
Mechanical Engineering, University of  
Texas, Rio Grande Valley, 1201 W  
University Dr., Edinburg, TX 78539, USA.  
Email: mataz.alcoutlabi@utrgv.edu

## Funding information

Welch Foundation, Grant/Award  
Number: BX-0048; NSF PREM, Grant/  
Award Number: DMR-2122178

\*Gregory B. McKenna Virtual Issue

## Abstract

SnO<sub>2</sub>/TiO<sub>2</sub> micro belt-fiber composites were successfully synthesized using centrifugal spinning and subsequent heat treatment of SnO<sub>2</sub>/TiO<sub>2</sub>/polyvinylpyrrolidone (PVP) precursor fibers. SnO<sub>2</sub>/TiO<sub>2</sub>/PVP precursor solutions consisting of different ratios of SnO<sub>2</sub> to TiO<sub>2</sub> were prepared by mixing Tin (II) 2-ethylhexanoate and titanium (IV) butoxide with PVP in ethanol. The SnO<sub>2</sub>/TiO<sub>2</sub>/PVP mixture was heat treated in air at 700°C, which resulted in the formation of SnO<sub>2</sub>/TiO<sub>2</sub> micron-sized fibers with a belt-shaped morphology. Structural, morphology, and surface chemistry characterization of the materials was performed using powder X-ray diffraction, scanning electron microscopy (SEM)/energy-dispersive X-ray spectrometer, and X-ray photoelectron spectroscopy analyses. SEM analysis showed the SnO<sub>2</sub>/TiO<sub>2</sub> composite fibers with (3:2) ratio had a micro belt morphology with particles on the surface. The material was tested as an anode material for lithium-ion batteries (LIBs); the composite fiber electrode delivered an initial capacity of 1200 mAh g<sup>-1</sup> at 100 mA g<sup>-1</sup>. The capacity was observed to decrease to 279 mAh g<sup>-1</sup> after 70 cycles; however, the sample retained a columbic efficiency of 99%, which indicated good reversibility. Due to the high surface area and unique structure, the as-synthesized SnO<sub>2</sub>/TiO<sub>2</sub> composite fibers may be promising for sensor and LIB applications.

## KEYWORDS

anode, centrifugal spinning, nanocomposites, nanofibers, SnO<sub>2</sub>, TiO<sub>2</sub>

## 1 | INTRODUCTION

Current advancements in nanotechnology have enabled the manufacturing of new nanocomposites with unique microstructures and morphologies. For example, porous, hollow, and tubular are features of the different structures that have been achieved through nanocomposite production methods, which include centrifugal spinning,

melt blowing, and electrospinning.<sup>[1-7]</sup> Due to the distinct characteristics and high surface area, nanocomposites have demonstrated improved performance in a wide variety of applications compared to their bulk counterpart.<sup>[8-10]</sup> Due to their semiconductive, photolytic, and electrochemical characteristics, SnO<sub>2</sub>/TiO<sub>2</sub> composites are among the most popular metal oxides that have been studied in the fields of energy storage, chemical sensing,

as well as in biomedical applications.<sup>[10–13]</sup> Furthermore, their low cost, abundance, and environmental friendliness are properties of SnO<sub>2</sub>/TiO<sub>2</sub> nanocomposites, which enable these materials to be considered for numerous battery and gas-sensing applications.<sup>[14–17]</sup>

Battery applications are of particular interest to develop better anode materials with specific morphologies. For example, Cheong et al. synthesized SnO<sub>2</sub>/TiO<sub>2</sub> fiber nanostructures with a tubular morphology through electrospinning followed by calcination. As an anode material for lithium-ion batteries (LIBs),<sup>[18,19]</sup> SnO<sub>2</sub>/TiO<sub>2</sub> composite fibers demonstrated good cycling stability and have surpassed the theoretical capacity of commercial graphite anodes. The SnO<sub>2</sub>/TiO<sub>2</sub> tubular nanocomposite delivered a high reversible capacity of 900 mAh g<sup>−1</sup> after 100 cycles at a current rate of 500 mA g<sup>−1</sup>.<sup>[17]</sup> Liang et al. synthesized SnO<sub>2</sub>/TiO<sub>2</sub> hollow-nanotube composites via sol–gel methodology. The sol–gel synthesized SnO<sub>2</sub>/TiO<sub>2</sub> nanocomposite was studied as an anode material for sodium-ion batteries (SIBs), which exhibited a high reversible sodium storage capacity of 316 mAh g<sup>−1</sup> after 50 cycles at 50 mA g<sup>−1</sup> and as a result of its hollow nanostructure. Furthermore, the SnO<sub>2</sub>/TiO<sub>2</sub> nanotubes demonstrated a good cycling capability at higher current rates.<sup>[20]</sup> In addition, Kunquan et al. have synthesized SnO<sub>2</sub>/TiO<sub>2</sub> short-fiber composites by electrospinning of a PVP/ceramic precursor solution followed by calcination in air. The composite fibers demonstrated improved gas-sensing activity compared to pure SnO<sub>2</sub> and TiO<sub>2</sub> electrodes. The enhanced performance was attributed to the combination of properties from SnO<sub>2</sub> and TiO<sub>2</sub> and the synergistic effect of TiO<sub>2</sub> that resulted in a heterojunction network, which resulted in improved conductivity and thus enhanced gas-sensing properties.<sup>[11]</sup> Despite the good performance achieved through the incorporation of nano and micro composites into a wide variety of applications, large-scale production of nano/micro composite fibers is still a major challenge. Currently, the most popular method used in laboratory to produce composite fibers with distinct nano/micro structures is electrospinning.<sup>[21,22]</sup> Electrospinning is based on electrostatic interactions and has been known as one of the simplest methods to prepare both solid and hollow composite nanofibers.<sup>[17,23]</sup> Although electrospinning can produce fibers, this technique still raises concerns due to the high voltage needed to yield fibers as well as its low production rate. Such drawbacks limit the use of electrospinning for mass production of nano/micro fibers.<sup>[24]</sup> Centrifugal spinning is a new method that has been gaining popularity in the area of nano/microfiber processing and formation.<sup>[25–28]</sup> Unlike electrospinning, centrifugal spinning does not depend on high voltage and electric field to produce nano and micro composite fibers.

Instead, centrifugal spinning depends solely on centrifugal forces caused by the spinneret rotational speed to produce nano and micro fibers with high yield and in a short period of time.<sup>[24,29–31]</sup>

In the current study, the production of SnO<sub>2</sub>/TiO<sub>2</sub> short micro belt fibers by centrifugal spinning and subsequent thermal treatment is detailed. To the best of our knowledge, the short micro belt structure of SnO<sub>2</sub>/TiO<sub>2</sub> composites has never been reported through centrifugal spinning. Due to their unique morphology and high active material content, the SnO<sub>2</sub>/TiO<sub>2</sub> composite fibers with 3:2 (SnO<sub>2</sub>:TiO<sub>2</sub>) ratio show a promise for LIB applications. Preliminary results on their electrochemical performance were investigated in this work. For comparison, pure SnO<sub>2</sub> nanoparticles were also synthesized via a precipitation method,<sup>[32]</sup> and their electrochemical performance was also evaluated.

## 2 | EXPERIMENTAL

### 2.1 | Materials and characterization methodology

Absolute ethanol (200 proof), polyvinylpyrrolidone (PVP) with weight average molecular weight (MW) of 1,300,000 (99.5%), tin II 2ethylhexanate (92.5%–100%), titanium IV butoxide (97%), polyacrylonitrile with average Mw of 150,000, *N,N*-dimethyl formamide (DMF), super p carbon black, ethylene carbonate (EC), and dimethyl carbonate (DMC) were all purchased from Sigma-Aldrich (USA) and used without further modification. Commercial lithium foil, and lithium salt (LiPF<sub>6</sub>) were purchased from MTI (USA). Whatman glass microfibers were purchased from GE healthcare. Precursor fibers were prepared by centrifugal spinning using a FiberLab L1000 (FibeRio) operated at different spinneret rotational speeds. The morphology and elemental composition of the fibers were studied using scanning electron microscope (SEM) using a Sigma VP Carl Zeiss instrument, equipped with an energy-dispersive X-ray spectrometer (EDS) from EDAX (Mahwah, NJ). The thermal behavior of the precursor fibers was investigated by thermogravimetric analysis (TGA) with a heating rate of 5°C/min from 50°C to 700°C. X-ray diffraction (XRD) and X-ray photoelectron spectroscopy (XPS) analyses were performed to determine crystal structure/crystallization phase of the oxidized fibers and the surface chemistry of the fibers. XRD patterns were studied using a Rigaku Miniflex II X-ray Diffractometer equipped with a copper source (K<sub>α</sub> λ = 1.54 Å). XPS spectra were collected using Thermoscientific K-α instrument equipped with monochromatized Al K<sub>α</sub> radiation (1486.7 eV).



## 2.2 | Synthesis of short $\text{TiO}_2$ , $\text{SnO}_2$ , and $\text{SnO}_2/\text{TiO}_2$ microfibers

Short metal-oxide microfibers were synthesized through the calcination of centrifugally spun precursor fibers. Briefly, 3 g of PVP were dissolved in 17 g of ethanol, and the solution was stirred for 12 h at room temperature. Subsequently, 1.5 g of tin (II) 2 ethylhexanate (i.e., 50% weight of PVP in the solution) was added to the solution, and the mixture was stirred for an additional 12 h to obtain a homogeneous solution. The solution was centrifugally spun at 9000 RPM with a relative humidity of 55% to prepare the precursor fibers. Initially, 1.5 ml of the prepared solution was injected into the spinneret. The rotational speed of the spinneret was maintained at 9000 rpm for 2 min until the solution was finished. The pristine precursor fibers were heated in air at 700°C for 3 h with a heating rate of 2°C/min to yield  $\text{SnO}_2$  short fibers. To obtain pure  $\text{TiO}_2$  precursor fibers, the same process was used. Initially, 1.5 g of titanium (IV) butoxide was added

to prepare the precursor solution. The process was used to obtain the  $\text{SnO}_2/\text{TiO}_2$  composite precursor solutions, which were labeled as  $\text{SnO}_2/\text{TiO}_2$  (3:2) and  $\text{SnO}_2/\text{TiO}_2$  (1:1). Basically, for the 1:1  $\text{SnO}_2/\text{TiO}_2$  precursor solution, the weight of  $\text{SnO}_2$  and  $\text{TiO}_2$  was 0.75 and 0.75 g, respectively, while for the 3:2  $\text{SnO}_2/\text{TiO}_2$  precursor solution, the weight of  $\text{SnO}_2$  and  $\text{TiO}_2$  was 0.9 and 0.6 g, respectively. The  $\text{SnO}_2/\text{TiO}_2$  composite fibers were produced after calcination the  $\text{SnO}_2/\text{TiO}_2$  precursor fibers in air at 700°C for 3 h with a heating rate of 2°C/min. The processing method of the short metal oxide micro fibers is shown in Figure 1.

## 2.3 | Electrochemical measurements

### 2.3.1 | Anode preparation

The as-prepared  $\text{SnO}_2/\text{TiO}_2$  nanocomposite, with a ratio of 3:2, were crushed in a mortar and pestle, then 80% of

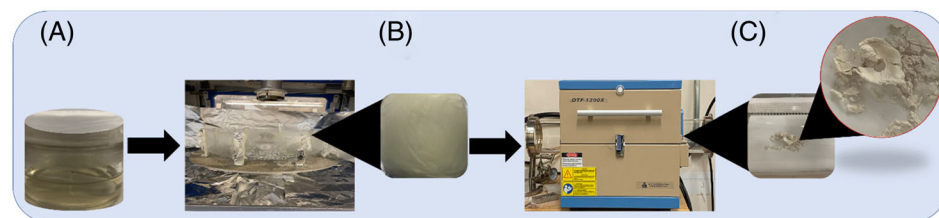


**FIGURE 1** A schematic representation of metal-oxides fiber fabrication process: (A) polymer solution with metal-oxide precursors, (B) centrifugal spinning, and (C) calcination

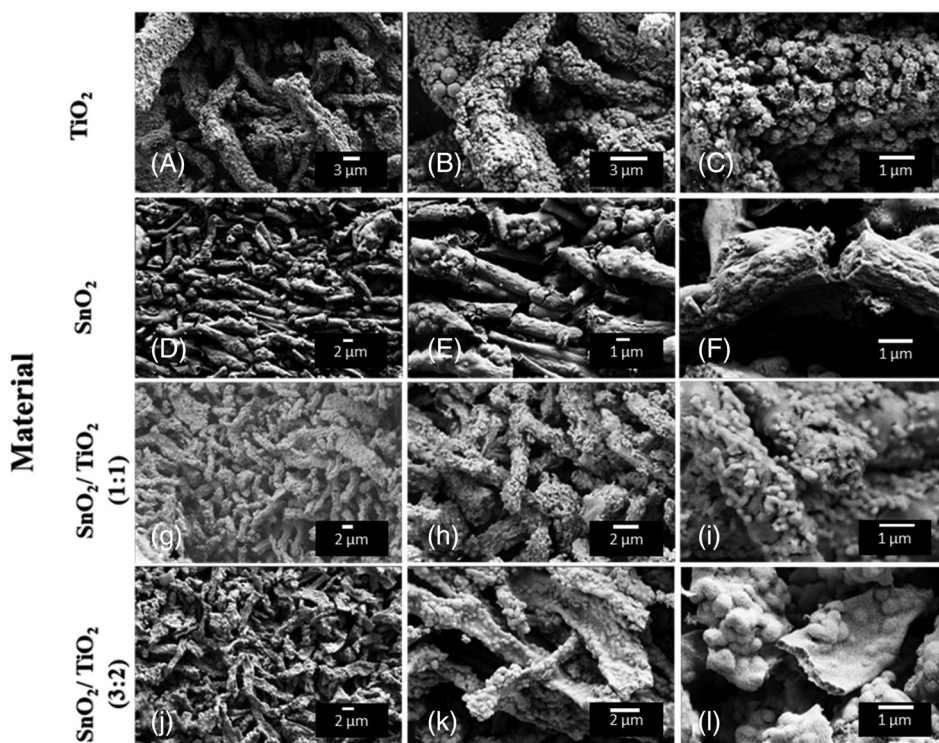


**FIGURE 2** SEM images of short nanofibers after calcination at 700°C:  $\text{TiO}_2$  (A–C),  $\text{SnO}_2$  (D–F),  $\text{SnO}_2/\text{TiO}_2$  (1:1) (G–I), and  $\text{SnO}_2/\text{TiO}_2$  (3:2) (J–L). Magnification: (A, D, G, J)  $\times 2000$ , (B, E, H, K)  $\times 5000$  and (C, F, I, L)  $\times 10,000$

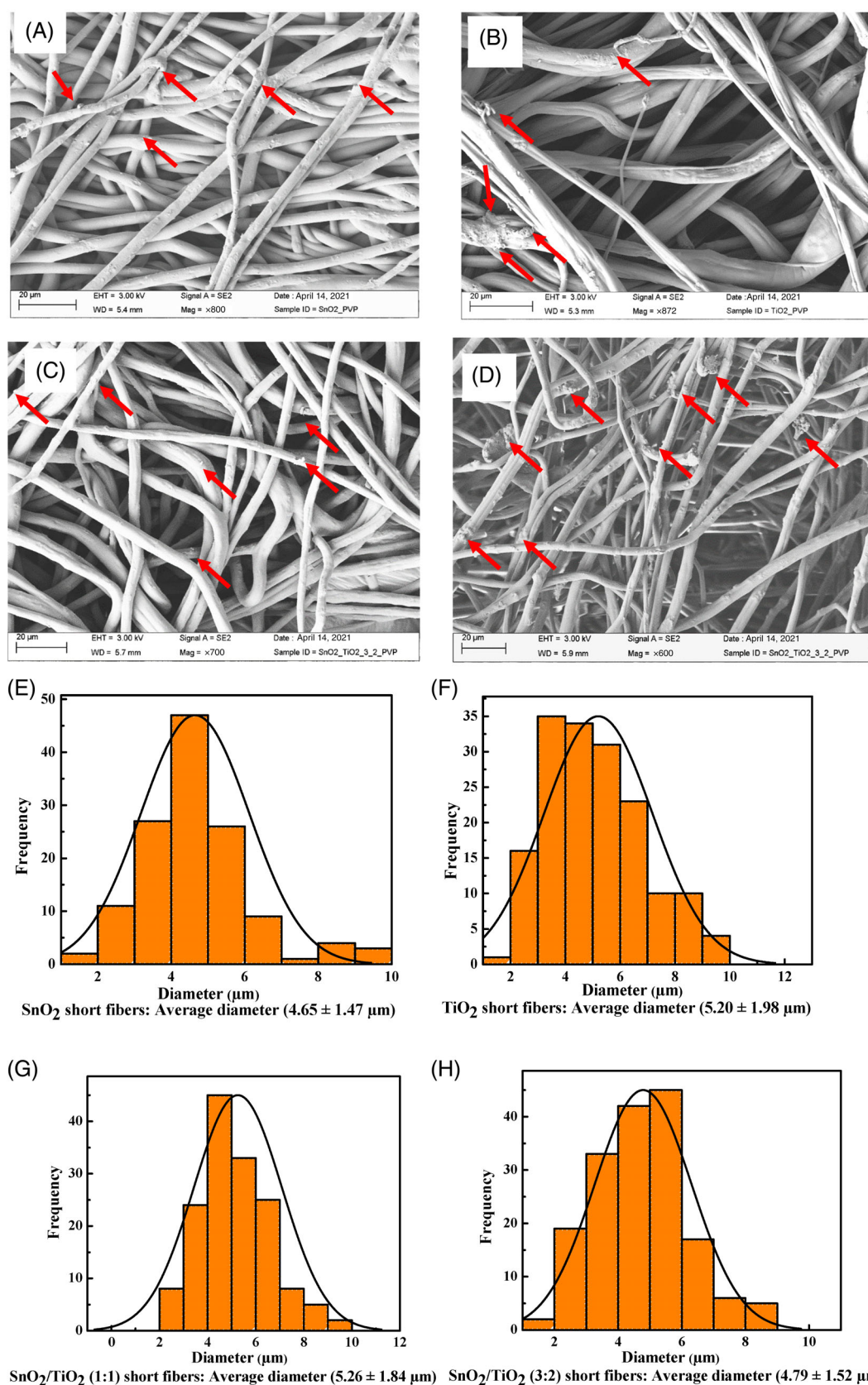


**FIGURE 3** SEM images of PVP precursor fibers containing: SnO<sub>2</sub> (A), TiO<sub>2</sub> (B), SnO<sub>2</sub>/TiO<sub>2</sub> (1:1) (C), and SnO<sub>2</sub>/TiO<sub>2</sub> (3:2) (D). Figure 3 (E, F, G, and H) represents the histograms of PVP precursor fibers containing SnO<sub>2</sub>, TiO<sub>2</sub>, SnO<sub>2</sub>/TiO<sub>2</sub> (1:1), and SnO<sub>2</sub>/TiO<sub>2</sub> (3:2), respectively. The red arrowhead indicates the location of nanoparticles on the fiber surface



the short fibers, 10% PAN, and 10% carbon black were mixed in 1 g of DMF to prepare a slurry. To obtain homogeneity, the as-prepared slurry was sonicated for 30 min and subsequently stirred for 12 h. After homogenization, the slurry was used to coat copper foil and dried under vacuum at 60°C for 24 h. Once dried, the coated slurry was heat treated in an argon-filled tube furnace at 450°C for 5 h with a heating rate of 2°C/min. After heating, 0.5" circles were cut to be tested as an anode material.

### 2.3.2 | Cell assembly

CR 2032 (PHD Energy Inc.) coin cells were used to assemble Li-ion half-cells in glove box under an argon atmosphere ( $O_2$ ,  $H_2O$  concentrations <0.5 ppm MBRAUN (USA). The as-prepared electrode as an anode material and Li-metal as the counter electrode, and a glass microfiber as a separator. The electrolyte was 1 M  $LiPF_6$  in ethylene carbonate (EC)/dimethyl carbonate (DMC) (1:1 v/v) without any further additives. Cyclic voltammetry experiments were performed, using Biologic Science Instruments (France), at a scan rate of 0.2 mV s<sup>-1</sup> over a voltage range between 0.05 and 3.0 V. Finally, the electrochemical performance was investigated through galvanostatic charge-discharge using a LANHE battery testing system (CT2001A) with an applied current density

of 100 mA g<sup>-1</sup> over 70 cycles over a potential range of 0.05–3.0 V.

## 3 | RESULTS AND DISCUSSION

### 3.1 | Characterization

Figure 2 shows the SEM images of the synthesized  $TiO_2$  (A–C),  $SnO_2$  (D–F),  $SnO_2/TiO_2$  (1:1) (G–I), and  $SnO_2/TiO_2$  (3:2) (J–L) nano/micro systems obtained after calcination at 700°C. As can be seen in Figure 2, the SEM images show short microfiber morphology with an average diameter between 4.65 and 5.26 mm (see histograms in Figure 3). In fact, the resultant oxidized fibers were composed of interconnected nanoparticles of metal oxides. The fiber length as observed in Figure 2 is the micron size range. The  $TiO_2$  sample (Figure 2A–C) exhibits short fiber porous structure and rough surface composed of nanoparticles. The SEM images of the  $SnO_2$  fibers (Figure 2D–F) depict a short fiber morphology with a smoother surface and nanoparticles randomly embedded in the surface. The  $SnO_2/TiO_2$  (1:1) composite fibers also adhere to a short-fiber structure morphology with smaller diameter interconnected nanoparticles on their surface as can be seen in Figure 2G–I. In comparison, the  $SnO_2/TiO_2$  (3:2) composite fibers show a different

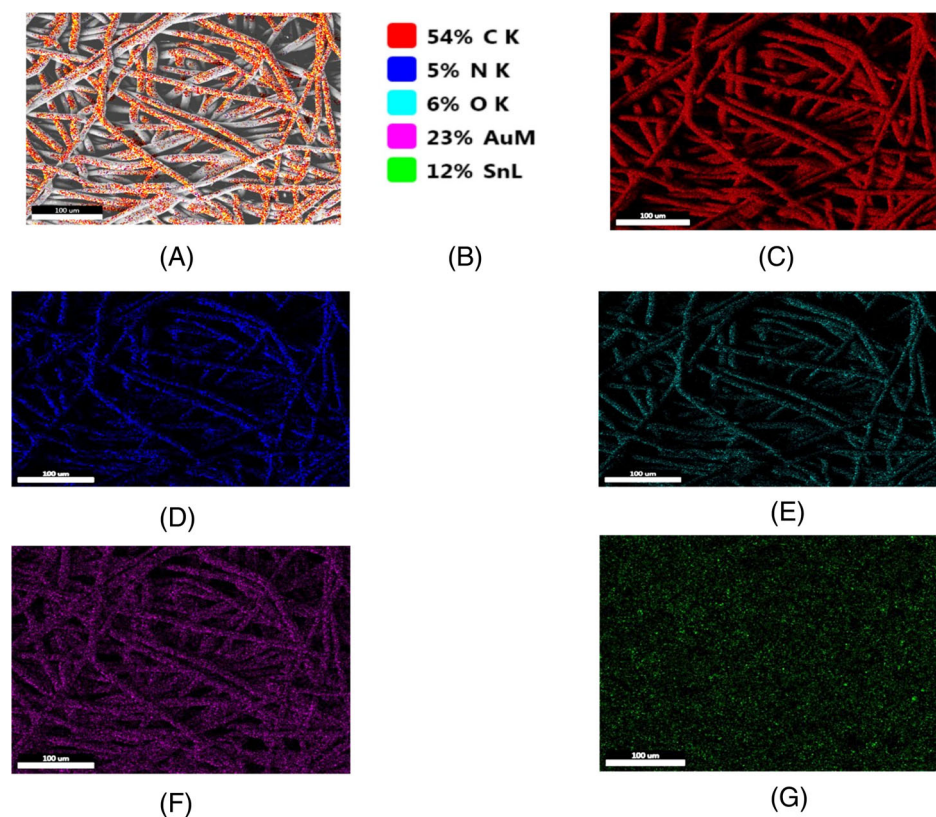


**FIGURE 4** EDS mappings of PVP/ $SnO_2$  precursor fibers before calcination (A) PVP/ $SnO_2$  sample, (B) percentage of different elements, (C) C, (D) N, (E) O, (F) Au, and (G) Sn

microstructure, which can be seen in Figure 2J–L. The SEM images of the  $\text{SiO}_2/\text{TiO}_2$  (3:2) composite reveals a short micro belt–fiber structure with nanoparticles randomly distributed on the surface. The morphology of  $\text{SnO}_2/\text{TiO}_2$  (3:2) composite fibers (Figure 2J–L is different from that of  $\text{SnO}_2$ ,  $\text{TiO}_2$ , and  $\text{SnO}_2/\text{TiO}_2$  (1:1) fibers. In fact, upon increasing the concentration of  $\text{SnO}_2$  in the  $\text{SnO}_2/\text{TiO}_2/\text{PVP}$  precursor solution, the  $\text{SnO}_2/\text{TiO}_2$  (1:1) composite fibers (after calcination) tended to change their morphology to flat ribbons (i.e., nanobelts). The increase in the precursor solution concentration (due to the increase in  $\text{SnO}_2$  concentration) might have shifted the morphology from circular to flat fibers. It was reported that increasing the solution viscosity until a critical intrinsic viscosity led to an increase in fiber diameter and interfiber spacing and a gradual shift in the morphology from circular to flat fibers.<sup>[33]</sup> In fact, increasing the solution viscosity results in reduced solvent evaporation rate leading the wet polymer jet to be deposited on the collector as flat fibers.<sup>[34]</sup> Another reason might affect the formation of flat fibers is the thermal treatment used in the calcination of the precursor fibers. It was reported that electrospun  $\text{SnO}_2$  flat fibers

( $\text{SnO}_2$  nanobelts) were formed after the calcination of the  $\text{PEO}/\text{SnO}_2$  precursor fibers in air at different temperatures between  $50^\circ\text{C}$  and  $1100^\circ\text{C}$ .<sup>[35]</sup> Understanding the formation of flat fibers and/or nanobelts after the calcination of the  $\text{SnO}_2/\text{TiO}_2/\text{PVP}$  precursor fibers requires more work. The average grain size for the  $\text{SnO}_2/\text{TiO}_2$  composite materials (Figure 2) determined using Scherrer's equation shows that the Sn phase was 38 nm and the  $\text{TiO}_2$  phase was 16 nm. The dispersion of nanoparticles on the electrode surface can be improved by using different techniques such as importing a surfactant and using an ultrasonic bath. It has been shown in the literature that the match between the radius of gyration of the polymer and nanoparticle size has been successful in the dissolution of nanoparticles into polymers.<sup>[36]</sup> The casting solvent has also been shown to influence the dispersion or homogeneity of composite material.<sup>[37]</sup> The dispersion of the nanoparticles in the polymer matrix has also been shown to be a combination of forces, which include the following: short-range van der Waals (VDW), long-range electrostatic repulsion, steric repulsion, and polymer-induced depletion attraction. The nature of solvent and of the polymer can play

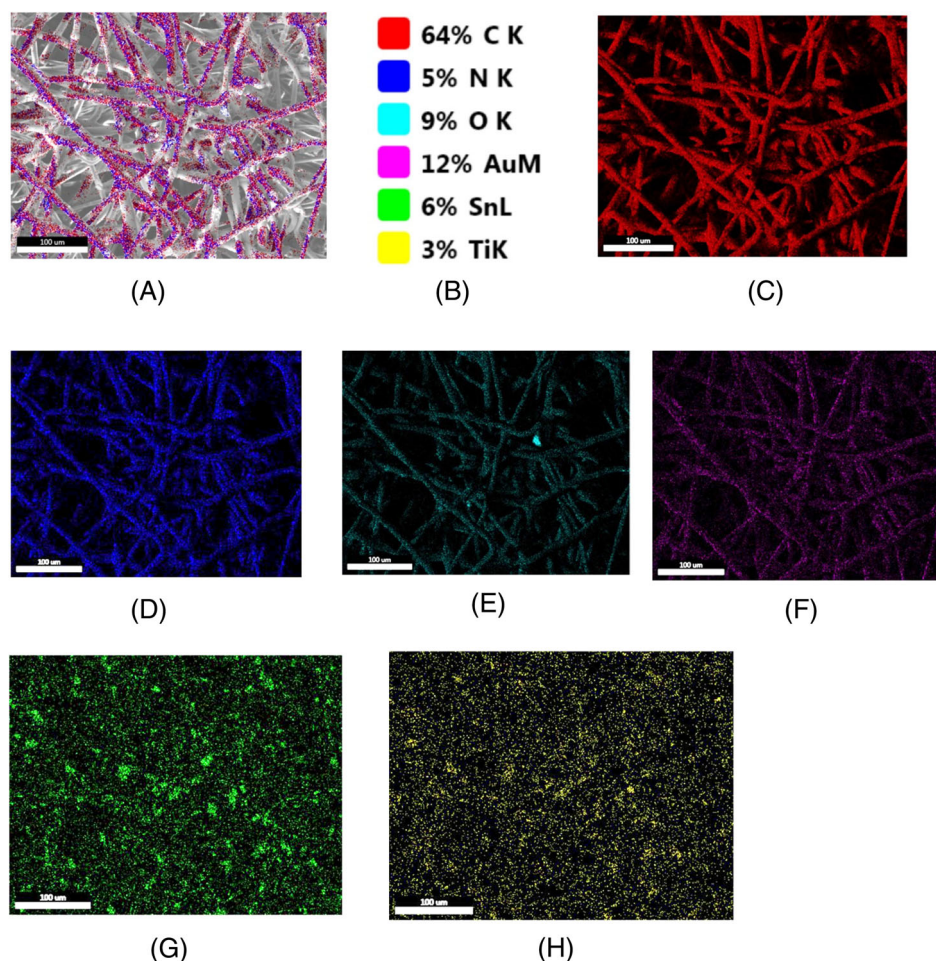


**FIGURE 5** EDS mappings of  $\text{SnO}_2/\text{TiO}_2$  (3:2) precursor fibers before calcination (A) PVP/ $\text{SnO}_2$  / $\text{TiO}_2$  sample, (B) percentage of different elements, (C) C, (D) N, (E) O, (F) Au (G) Sn, and (H) Ti

a major role and affect each of these forces, thus the final NP stability.<sup>[37]</sup>

SEM images and histograms of PVP/ceramic precursor fibers are shown in Figure 3. The PVP/SnO<sub>2</sub> precursor fibers (Figure 3A) have cylindrical shape, while the fibers are more attached to each other. Additionally, the PVP/SnO<sub>2</sub> nanofibers have smaller average diameter than that for TiO<sub>2</sub> fibers (Figure 3A,B) due to the

enhanced dispersion of Ti nanoparticles in the precursor solution compared to that of Sn. For this reason, based on the histograms of these two precursor fibers (Figure 3E,F), the SnO<sub>2</sub> fibers had smaller average diameter than that for the TiO<sub>2</sub> fibers. However, the round cross-section of both fibers was attributed to the sufficient evaporation time that took place during centrifugal spinning of the precursor solutions at ambient conditions. In

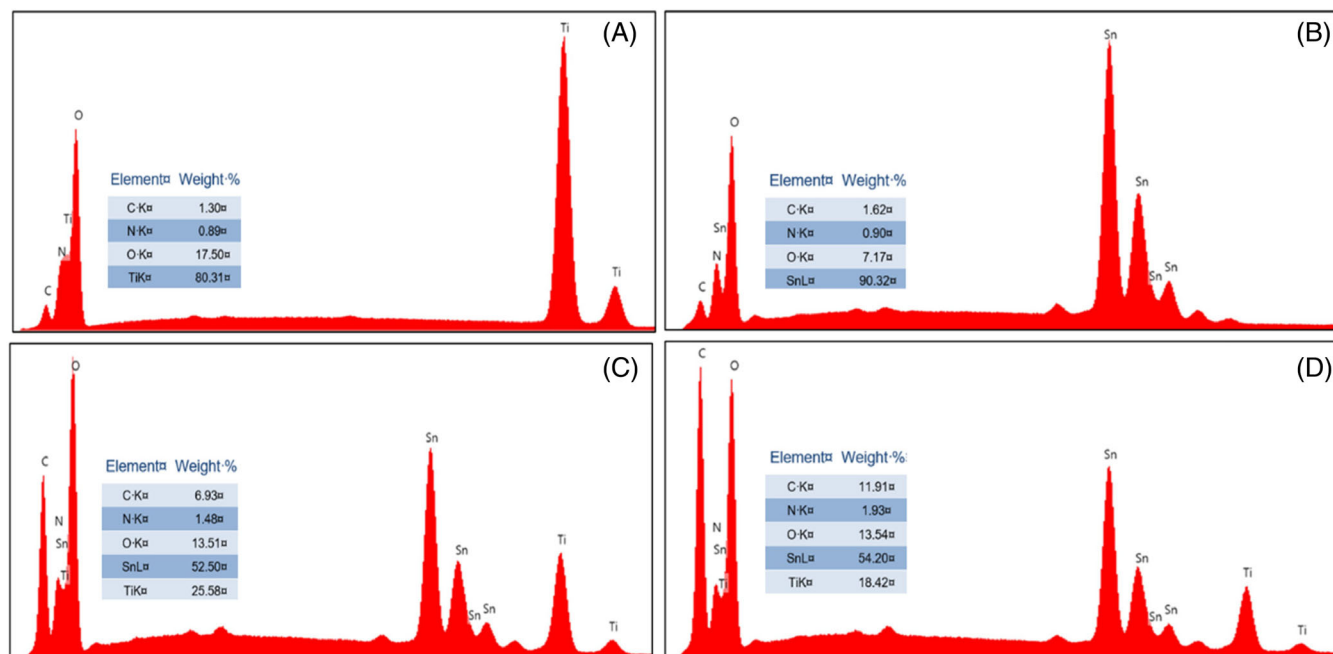


FIGURE 6 EDS spectrum of TiO<sub>2</sub> (A) SnO<sub>2</sub> (B), SnO<sub>2</sub>/TiO<sub>2</sub> (1:1) (C), and SnO<sub>2</sub>/TiO<sub>2</sub> (3:2) (D) after calcination at 700°C

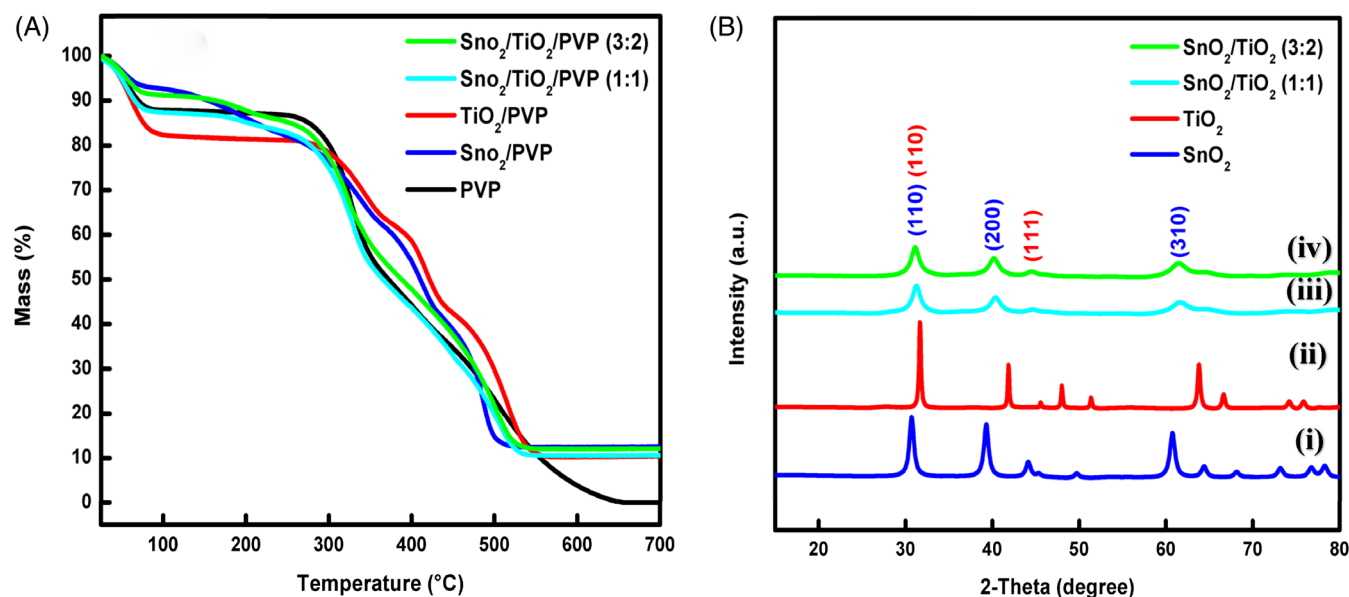


FIGURE 7 TGA (A) of PVP and pristine fibers before calcination, XRD (B), of TiO<sub>2</sub> (i), SnO<sub>2</sub> (ii), SnO<sub>2</sub>/TiO<sub>2</sub> (1:1) (iii), and SnO<sub>2</sub>/TiO<sub>2</sub> (3:2) (iv) after calcination at 700°C



fact, if the fibers were swollen with solvent, then they would have cylindrical shape regardless of the evaporation time as long as the viscosity of the precursor solution does not exceed the critical intrinsic viscosity of the solution.<sup>[33]</sup> Moreover, the presence of Sn and Ti nanoparticles is apparent on the fibrous surface as indicated to white spots (marked by red arrowhead), while the density of Sn nanoparticles on the surface is larger than that for Ti nanoparticles.

Regarding the SnO<sub>2</sub>/TiO<sub>2</sub> fibers with 1:1 and 3:2 ratios, the average diameter of the latter is larger than 1:1, which was attributed to more SnO<sub>2</sub> were deposited within the interior of the fibers. For this reason, there are several defected flat portions on the (3:2) SnO<sub>2</sub>/TiO<sub>2</sub> fibrous surface, which determined that the more portion of Sn in the precursor fibers, the more abrupt solidification of fibers. Above all, the fibers with cylindrical morphology, observed in both SEM images, concluded that at ambient conditions, the fibers are very smooth at given spinning runtime and rotational speed.

The elemental composition of the composite microfibers was studied by EDS. Figures 4 and 5 show EDS mappings of PVP/SnO<sub>2</sub> and PVP/SnO<sub>2</sub>/TiO<sub>2</sub>

precursor fibers, while Figure 6 shows EDS spectra of TiO<sub>2</sub>, SnO<sub>2</sub>, SnO<sub>2</sub>/TiO<sub>2</sub> (1:1), and SnO<sub>2</sub>/TiO<sub>2</sub> (3:2) composite fibers after calcination at 700°C.

EDS mappings of PVP/SnO<sub>2</sub> and PVP/SnO<sub>2</sub>/TiO<sub>2</sub> precursor fibers (Figures 4 and 5) confirm that Sn, Ti, O, N, C, and Au (presence due to gold sputtering the fibers prior to SEM) were highly present within the elemental composition of each corresponding sample. As shown in Figure 4A–G that the SnO<sub>2</sub> precursor fibers had 12 wt% of Sn, while the SnO<sub>2</sub>/TiO<sub>2</sub> (3:2) precursor fibers (Figure 5, A–H) had only 6 and 3 wt% of Sn and Ti, respectively. In addition, the PVP/SnO<sub>2</sub> sample (Figure 4) showed 54 wt% of C, while the SnO<sub>2</sub>/TiO<sub>2</sub> (3:2) precursor fibers showed 64 wt% of C, respectively. Therefore, the presence of a higher ratio of SnO<sub>2</sub>:TiO<sub>2</sub>, basically assists with increasing the wt% of C in the SnO<sub>2</sub>/TiO<sub>2</sub> (3:2) precursor fibers. The small differences in the amount of Sn and Ti observed within the SnO<sub>2</sub>/TiO<sub>2</sub> composite-fiber samples with 1:1 and 3:2 (SnO<sub>2</sub>:TiO<sub>2</sub>) ratios compared to the ideal ratios are ascribed to the successful mixing of SnO<sub>2</sub> and TiO<sub>2</sub> in the precursors.

In the EDS spectrum of Figure 6A, the TiO<sub>2</sub> sample exhibited a high content of 80 wt% of Ti, while the SnO<sub>2</sub>/

**TABLE 1** Le bail fitting SnO<sub>2</sub>, TiO<sub>2</sub>, and SnO<sub>2</sub>/TiO<sub>2</sub> samples

Sample	Phase	Space group	a (Å)	b (Å)	c (Å)	α (°)	β (°)	γ (°)	χ <sup>2</sup>
SnO <sub>2</sub> 700°C	SnO <sub>2</sub>	P 42/m n m	4.732 (7)	4.732 (7)	3.132 (9)	90.00	90.00	90.00	2.44
TiO <sub>2</sub> 700°C	TiO <sub>2</sub>	P 42/m n m	4.589 (9)	4.589 (9)	2.957 (2)	90.00	90.00	90.00	3.04
	TiO <sub>2</sub>	P 42/m n m	4.600 (2)	4.600 (2)	2.98 (2)	90.00	90.00	90.00	
SnO <sub>2</sub> /TiO <sub>2</sub> 700°C 1:1	TiO <sub>2</sub>	P 42/m n m	4.518 (1)	4.518 (1)	2.959 (2)	90.00	90.00	90.00	2.08
	SnO <sub>2</sub>	P 42/m n m	4.7454 (4)	4.745 (4)	3.130 (9)	90.00	90.00	90.00	
SnO <sub>2</sub> /TiO <sub>2</sub> 700°C 3:2	TiO <sub>2</sub>	P 42/m n m	4.544 (2)	4.544 (2)	2.950 (0)	90.00	90.00	90.00	1.82
	SnO <sub>2</sub>	P 42/m n m	4.741 (6)	4.741 (6)	3.133 (9)	90.00	90.00	90.00	

**TABLE 2** Observed diffraction planes in the TiO<sub>2</sub>, SnO<sub>2</sub>, and TiO<sub>2</sub>/SnO<sub>2</sub> composite samples

2θ (°)	Miller indices TiO <sub>2</sub>	2θ (°)	Miller indices SnO <sub>2</sub>	2θ (°)	Miller indices TiO <sub>2</sub> /SnO <sub>2</sub>
32.1	110	31.0	110	31.2	110/110
42.3	101	39.7	101	40.3	101/101
45.8	200	44.6	200	44.5	200/200
48.3	111	45.6	111	61.7	210/210
61.6	210	61.0	210	74.00	002/002
64.3	211	64.8	2111	78.50	301
67.0	220	68.9	220		
74.6	002	73.6	002		
76.1	310/221	74.3	310/221		
		77.1	112		
		78.8	301		

TiO<sub>2</sub> composites with 1:1 and 3:2 (SnO<sub>2</sub>:TiO<sub>2</sub>) ratios only depict 25 and 18 wt% of Ti, respectively. In addition, the pure SnO<sub>2</sub> sample (Figure 6B) showed 90 wt% of Sn, while the SnO<sub>2</sub>/TiO<sub>2</sub> composites with 1:1 and 3:2 (SnO<sub>2</sub>:TiO<sub>2</sub>) ratios showed 52 and 54 wt% of Sn, respectively. Furthermore, the EDS spectrum of all samples exhibited signal peaks of oxygen, which confirm the presence of SnO<sub>2</sub> and TiO<sub>2</sub> in the as-synthesized samples. However, carbon and nitrogen signals can also be observed in all samples. These small signals found are attributed to precursor impurities, carbon residue from the PVP, and the carbon tape used during sample preparation.<sup>[38]</sup>

Figure 7A shows the TGA results of the composite precursor fibers as well as the PVP fibers. As can be seen in Figure 7A, all composite precursor fibers have two main weight loss steps observed in two different

temperature ranges. The first weight loss was observed in the range of 25°C–100°C, which can be attributed to the loss of either remaining solvent or water adsorbed within the fibers. The second observed weight loss between 300°C and 550°C can be associated with the degradation of the polymer and ceramic precursor in the fibers. At the temperature range between 560°C and 700°C, the samples show stable and constant average of residual weight of 10 wt%, which was attributed to the formation of SnO<sub>2</sub>, TiO<sub>2</sub>, and SnO<sub>2</sub>/TiO<sub>2</sub> composites as well as carbon residue, and so forth. Figure 7B shows diffraction patterns for the SnO<sub>2</sub> (i), TiO<sub>2</sub> (ii), SnO<sub>2</sub>/TiO<sub>2</sub> (1:1) (iii), SnO<sub>2</sub>/TiO<sub>2</sub> (3:2), and (iv) short microfibers. The SnO<sub>2</sub> (i) and TiO<sub>2</sub> (ii) samples have similar lattices, which was the P42/M space group, and each lattice has different lengths to the sides of the unit cell. The results of the Le

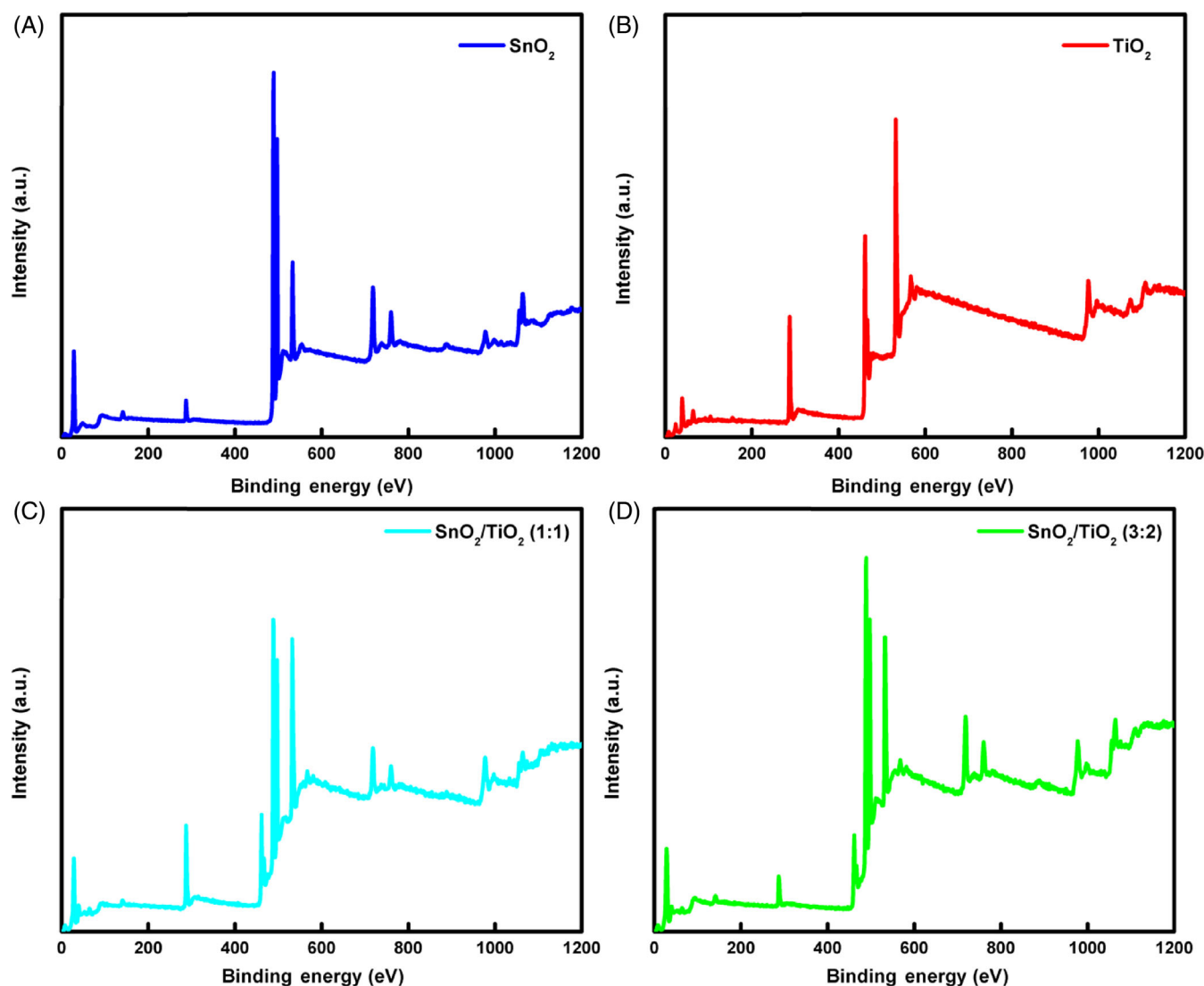


FIGURE 8 XPS surveys for the SnO<sub>2</sub> oxidized short fibers at 700°C (A), SnO<sub>2</sub>:TiO<sub>2</sub> with a ratio of 1:1 (B) and SnO<sub>2</sub>:TiO<sub>2</sub> at a ratio of 3:2 (C)

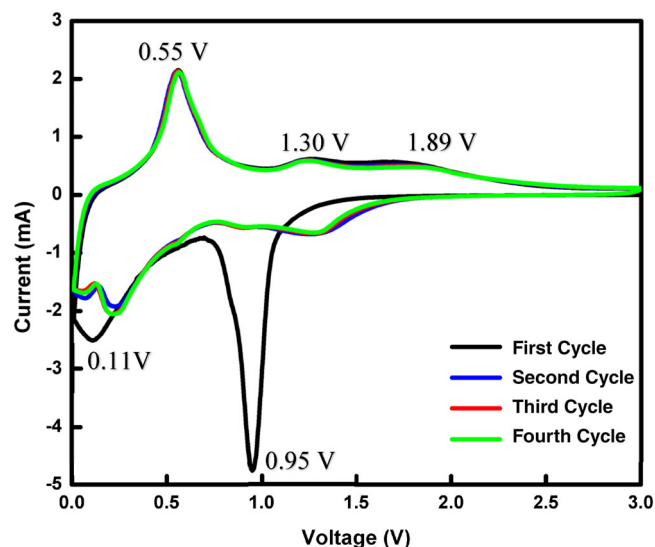


FIGURE 9 Cyclic voltammetry of  $\text{SnO}_2/\text{TiO}_2$  composite fibers with 3:2 ( $\text{SnO}_2:\text{TiO}_2$ ) ratio

Bail fitting are shown in Table 1, which indicates that a good fitting was obtained between the known structure of  $\text{TiO}_2$  and  $\text{SnO}_2$  and the synthesized samples; the GOF is indicated by a  $\chi^2$  value of less than 5. The diffraction patterns of the  $\text{TiO}_2$ ,  $\text{SnO}_2$ , and  $\text{SnO}_2/\text{TiO}_2$  fibers are shown in Table 2. The fitting results confirmed both rutile ( $\text{TiO}_2$ ) and  $\text{SnO}_2$ .<sup>[39–43]</sup> In addition, the peaks in the diffraction patterns for the composite-fiber samples were broad and weak when compared to the peaks in diffraction patterns of the  $\text{TiO}_2$  and  $\text{SnO}_2$  fibers. The presence of broad and weak diffraction peaks is typically indicative of the presence of nanoparticles or small crystallites.

X-ray photoelectron (XPS) characterization was performed to determine the compositions and chemical states of the elemental components in the samples. XPS survey spectrum for each sample is shown in Figure 8A–D, which shows the presence of Sn and O as the major components in the  $\text{SnO}_2$  sample and some

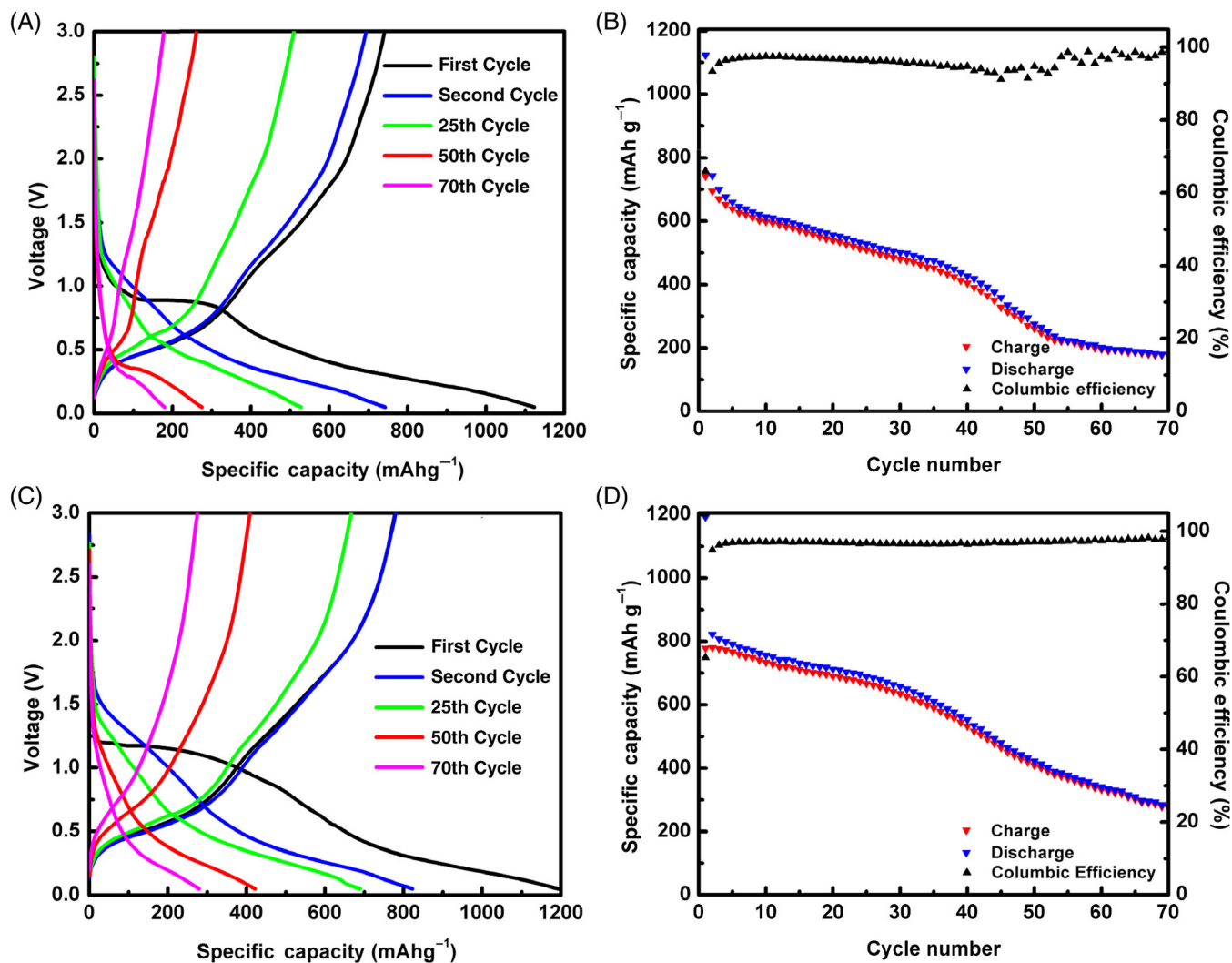


FIGURE 10 Charge/discharge curves and profiles of pure  $\text{SnO}_2$  fibers (A, B) and  $\text{SnO}_2/\text{TiO}_2$  short fibers at a ratio of 3:2 (C, D)



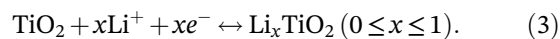
residual C from the sample preparation. The XPS spectrum of the TiO<sub>2</sub> fibers shows the presence of Ti and oxygen as the main portions of the sample with some residual carbon left from the synthesis. A detailed discussion on the XPS results for the Sn, Ti, C, O, and N spectra of all materials is given in Appendix S1 (See Figures [S1, S2, and S3] and discussion).

### 3.2 | Electrochemical performance

To determine the reduction/oxidation reactions of the anode electrode, CV experiments were performed over a voltage range of 0.05–3.0 V and at a scan rate of 0.2 mVs<sup>-1</sup> over four cycles. Figure 9 shows the cyclic voltammetry curves of the SnO<sub>2</sub>/TiO<sub>2</sub> micro belt fibers with 3:2 (SnO<sub>2</sub>:TiO<sub>2</sub>) ratio. The electrochemical performance was only evaluated for the SnO<sub>2</sub>/TiO<sub>2</sub> composite fibers with 3:2 (SnO<sub>2</sub>:TiO<sub>2</sub>) ratio due to their structure and morphology (i.e., micro belt or flat fibers, Figure 2J–L), compared to that with 1:1 (SnO<sub>2</sub>:TiO<sub>2</sub>) ratio (i.e., cylindrical-type morphology). In addition, the composite fibers with 3:2 (SnO<sub>2</sub>:TiO<sub>2</sub>) ratio should have more SnO<sub>2</sub> content than that for the 1:1 ratio, which can result in higher capacities.<sup>[39]</sup>

During the first cycle, the peaks at 0.95, 0.11, and 0.55 V can be attributed to the formation of the solid electrolyte interface (SEI), electrolyte decomposition, and the dealloying process generating Li<sub>x</sub>Sn, respectively.<sup>[44–46]</sup> Furthermore, the redox peak at 1.3 V is ascribed to the reversible conversion reaction of Sn and LiO<sub>2</sub> to form SnO<sub>2</sub>, while the peak at 1.89 V is attributed to the insertion/extraction of lithium from TiO<sub>2</sub>. From the second

cycle and beyond, the CV curves coincide with each other, indicating high reversibility and good cycling performance of the anode electrode. The process illustrated by the CV curves can be chemically represented by the following Equations<sup>[44–46]</sup>:



The cycle performance of SnO<sub>2</sub> fibers and the SnO<sub>2</sub>/TiO<sub>2</sub> micro belt fibers with a ratio of 3:2 was evaluated using galvanostatic experiments at a current density of 100 mA g<sup>-1</sup> for 70 cycles over a voltage range of 0.05–3.0 V (Figure 10A,B and C,D, respectively). Initially, the SnO<sub>2</sub> fibers demonstrated irreversible discharge capacity of 1123 mAh g<sup>-1</sup> and charge capacity of 741 mAh g<sup>-1</sup>; however, the reversible capacity after 70 cycles dropped to 179 mAh g<sup>-1</sup>. Such a capacity reduction was attributed to the pulverization and instability of SnO<sub>2</sub> upon cycling caused by the high-volume change developed during lithium insertion/extraction. On the other hand, the SnO<sub>2</sub>/TiO<sub>2</sub> micro belt fibers (3:2 ratio) demonstrated high but irreversible discharge capacity of 1200 mAh g<sup>-1</sup> and charge capacity of 820 mAh g<sup>-1</sup> during the first cycle, resulting in a coulombic efficiency of 65%. Such an irreversible capacity can be attributed to the formation of the SEI at the anode/electrode interface. At the second cycle, the reversible capacity of the SnO<sub>2</sub>/TiO<sub>2</sub> micro belt fibers (3:2 ratio) decreased to 700 mAh g<sup>-1</sup> (Figure 10C), which is

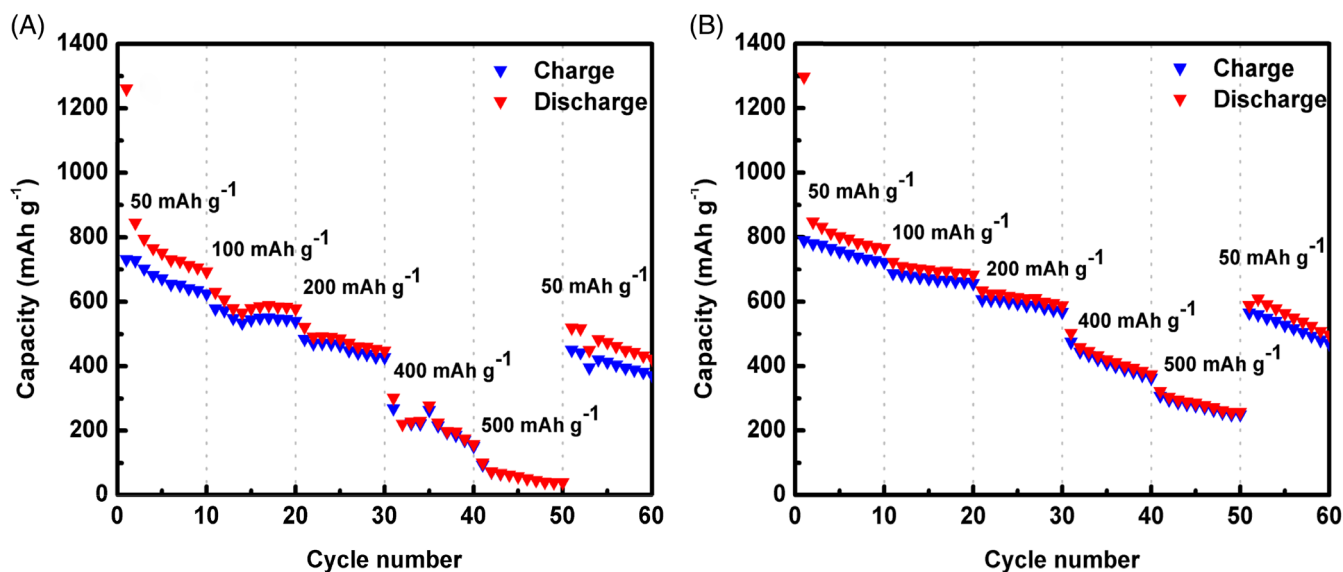


FIGURE 11 Rate performance of pure SnO<sub>2</sub> fibers (A) and SnO<sub>2</sub>/TiO<sub>2</sub> short fibers with 3:2 (SnO<sub>2</sub>:TiO<sub>2</sub>) ratio (B)

higher than the theoretical capacity of graphite anode ( $372 \text{ mAh g}^{-1}$ ). However, after 70 cycles, the capacity decreased to  $279 \text{ mAh g}^{-1}$ . Such a drastic drop in capacity can be attributed to inevitable pulverization of the anode upon cycling caused by internal stresses (volume change) during lithiation/de-lithiation. Despite this reduction, the electrode retained a high coulombic efficiency of 99% after 70 cycles indicating good reversibility. When comparing the pure  $\text{SnO}_2$  fibers to the  $\text{SnO}_2/\text{TiO}_2$  micro belt fibers with a ratio of 3:2 (Figure 10A,B), it was obvious that the  $\text{SnO}_2/\text{TiO}_2$  short fibers demonstrated less volume expansion due to the addition of  $\text{TiO}_2$  and also to its unique micro belt structure. Such attributes mitigated the internal stresses experienced upon cycling, which resulted in less capacity retention and higher reversible capacity after 70 cycles.

In fact, the anodes prepared from  $\text{SnO}_2$  and  $\text{SnO}_2/\text{TiO}_2$  short fibers showed relatively poor performance (Figure 10A–D). This is caused by the high-volume change of the  $\text{SnO}_2$  fibers after prolonged charge/discharge cycles. The formation of the SEI layer at the first discharge cycle (Li-alloying) can also contribute to the low capacity at the first charge (Li-dealloying) cycle. The low Coulombic efficiency of the anodes at the first cycle (Figure 10B,D) is caused by the formation of the SEI layer in the first cycle and the decomposition of the electrolyte at the anode surface. In fact, a thick SEI layer can consume a large amount of Li ions and electrolyte at the first discharge (Li-insertion) cycle, thus resulting in a high irreversible capacity and low ICE.<sup>[47,48]</sup>

The electrochemical performance of the  $\text{SnO}_2$  and  $\text{SnO}_2/\text{TiO}_2$  electrodes can be improved by coating the anode surface with carbon layer or by incorporating carbon-based material in the anode. For example, reducing the large volume change observed in Si, Sn, and metal oxide-based anodes has been achieved by coating the anode with flexible and highly conductive carbonaceous material.<sup>[49,50]</sup> The use of graphene with the  $\text{SnO}_2$  and  $\text{SnO}_2/\text{TiO}_2$  materials can also control the rapid degradation of the electrodes discussed in this work. The design of  $\text{SnO}_2/\text{C}$  and  $\text{SnO}_2/\text{TiO}_2/\text{C}$  composite nanofibers as anode for LIBs can also result in reduced volume change and improved electrochemical performance of the anode. There is ongoing work in our laboratory addressing these issues.

To further investigate the electrochemical performance and reversibility of the composites, the pure  $\text{SnO}_2$  and the  $\text{SnO}_2/\text{TiO}_2$  micro belt fibers anodes with a ratio of 3:2 were tested at different current rates (the rate performance results are shown Figures 11A,B, respectively). It can be observed that the  $\text{SnO}_2/\text{TiO}_2$  micro belt fibers delivered higher capacities than that of  $\text{SnO}_2$ -fiber anode at all current densities, indicating a good rate capability. When the current density reached  $500 \text{ mA g}^{-1}$ , the  $\text{SnO}_2$ -

fiber anode delivered a capacity just slightly more than  $0 \text{ mAh g}^{-1}$  while the micro belt fibers showed a capacity of  $250 \text{ mAh g}^{-1}$ . The performance can be attributed to the addition of  $\text{TiO}_2$ , which is known to have a good rate performance at high current rates due to its low volume change upon cycling. In addition, when the current density was brought back to  $50 \text{ mA g}^{-1}$ , the  $\text{SnO}_2/\text{TiO}_2$  short fibers showed better recovery than that of the  $\text{SnO}_2$  fiber anode. The  $\text{SnO}_2/\text{TiO}_2$  short-fiber anode exhibited improved rate capability and reversibility when compared to the pure  $\text{SnO}_2$  fibers.

## 4 | CONCLUSIONS


Short  $\text{SnO}_2/\text{TiO}_2$  micro belt fibers were successfully synthesized through safe, facile, and fast processing fiber production method. Short micro belt fibers were synthesized using tin and titanium precursors mixed in ethanol/PVP, which was used in the centrifugal spinning process. The calcination of the precursor fibers in air at  $700^\circ\text{C}$  resulted in a short micro belt fiber morphology with nanoparticles on the surface, which was observed by the SEM studies. Furthermore, the phases, stability, and elemental composition of  $\text{SnO}_2/\text{TiO}_2$  were confirmed using EDS, XPS, and TGA analysis. The XRD patterns confirmed the presence of crystal structure of  $\text{SnO}_2$  and the rutile phase of  $\text{TiO}_2$  within the fibers. In addition, when used as an anode material in LIBs, the  $\text{SnO}_2/\text{TiO}_2$  micro belt fibers demonstrated initial irreversible capacity of  $1200 \text{ mAh g}^{-1}$  and reversible charge capacity of  $820 \text{ mAh g}^{-1}$  when tested at a current rate of  $100 \text{ mA g}^{-1}$ . However, due to the pulverization of the anode upon cycling, the reversible capacity decreased to  $279 \text{ mAh g}^{-1}$  after 70 cycles. In addition, the  $\text{SnO}_2/\text{TiO}_2$  micro belt fibers demonstrated an enhanced rate capability when compared to pure  $\text{SnO}_2$  fibers, which was attributed to the presence of  $\text{TiO}_2$ . Aside from good electrochemical performance, the unique morphology, high active material content, and facile processing of the short micro belt fibers are properties that make these composite sort fibers good candidates to be considered for battery and sensor applications. Further work is needed to enhance the capacity retention over cycling, which could be improved by carbon coating the short metal oxide to prepare efficient ternary  $\text{SnO}_2/\text{TiO}_2/\text{C}$  composites for battery applications.

## ACKNOWLEDGMENTS

This work was the funding support received by NSF PREM award under grant No. DMR-2122178: UTRGV-UMN Partnership for Fostering Innovation by Bridging Excellence in Research and Student Success. Jason Parsons would like to acknowledge the support from the Department of Chemistry at the University of Texas Rio

Grande Valley and the generous support provided by a Departmental Grant from the Robert A. Welch Foundation (Grant No. BX-0048).

## ORCID

Mataz Alcoutlabi  <https://orcid.org/0000-0003-4641-9109>

## REFERENCES

- [1] W. K. Tan, H. Muto, G. Kawamura, Z. Lockman, A. Matsuda, *Nanomaterials* **2021**, *11*, 181.
- [2] A. Ślosarczyk, *Nanomaterials* **2021**, *11*, 258.
- [3] M. Pelzer, T. Vad, A. Becker, T. Gries, S. Markova, V. Teplyakov, *J. Appl. Polym. Sci.* **2021**, *138*, 49630.
- [4] A. Kotrotsos, *Polym. Eng. Sci.* **2021**, *61*, 5.
- [5] X. Wang, H. T. Niu, T. Lin, X. G. Wang, *Polym. Eng. Sci.* **2009**, *49*, 1582.
- [6] S. F. Xin, X. H. Wang, *Polym. Eng. Sci.* **2012**, *52*, 1325.
- [7] M. Gungor, M. N. Sagirli, M. D. Calisir, S. Selcuk, A. Kilic, *Polym. Eng. Sci.* **2021**, *61*, 2311. <https://doi.org/10.1002/pen.25759>
- [8] J. Lu, Z. Chen, Z. Ma, F. Pan, L. A. Curtiss, K. Amine, *Nat. Nanotechnol.* **2016**, *11*, 1031.
- [9] E. S. Pampal, E. Stojanovska, B. Simon, A. Kilic, *J. Power Sources* **2015**, *300*, 199.
- [10] K. Chen, M. Pi, D. Zhang, *J. Phys. D: Appl. Phys.* **2020**, *53*, 125301.
- [11] K. Chen, S. Chen, M. Pi, D. Zhang, *Solid-State Electron.* **2019**, *157*, 42.
- [12] H. Dzinun, M. H. D. Othman, A. F. Ismail, M. H. Puteh, M. A. Rahman, J. Jaafar, N. Adrus, N. A. Hashim, *Polym. Eng. Sci.* **2018**, *58*, 1636.
- [13] V. Aravindan, P. Vickraman, *Polym. Eng. Sci.* **2009**, *49*, 2109.
- [14] P. Kongsong, L. Sikong, S. Niyomwas, V. Rachpech, *Sci. World J.* **2014**, *2014*, 869706.
- [15] K. K. Akurati, A. Vital, R. Hany, B. Bommer, T. Graule, M. Winterer, *Int. J. Photoenergy* **2005**, *7*, 575146.
- [16] H. Shi, M. Zhou, D. Song, X. Pan, J. Fu, J. Zhou, S. Ma, T. Wang, *Ceram. Int.* **2014**, *40*, 10383–10393.
- [17] J. Y. Cheong, C. Kim, J.-W. Jung, T.-G. Yun, D. Y. Youn, S.-H. Cho, K. R. Yoon, H.-Y. Jang, S. W. Song, I.-D. Kim, *J. Power Sources* **2018**, *400*, 485.
- [18] M. Akia, L. Cremer, M. Seas, J. Villarreal, A. Valdez, M. Alcoutlabi, K. J. P. E. Lozano, *Polym. Eng. Sci.* **2018**, *58*, 2047.
- [19] M. Biso, R. Colombo, M. J. Uddin, M. Stanga, S. J. Cho, *Polym. Eng. Sci.* **2016**, *56*, 760.
- [20] J. Liang, L. Zhang, D. XiLi, J. Kang, *Electrochim. Acta* **2020**, *341*, 136030.
- [21] S. Hafner, H. Guthrey, S.-H. Lee, C. Ban, *J. Power Sources* **2019**, *431*, 17.
- [22] K. Javed, M. Oolo, N. Savest, A. Krumme, *Crit. Rev. Solid State Mater. Sci.* **2019**, *44*, 427.
- [23] Z. Li, Q. Yin, W. Hu, J. Zhang, J. Guo, J. Chen, T. Sun, C. Du, J. Shu, L. Yu, *J. Mater. Sci.* **2019**, *54*, 9025.
- [24] X. Zhang, Y. Lu, *Polym. Rev.* **2014**, *54*, 677.
- [25] L. Zuniga, G. Gonzalez, R. Orrostieta Chavez, J. C. Myers, T. P. Lodge, M. Alcoutlabi, *Appl Sci* **2019**, *9*, 4032.
- [26] L. Zuniga, V. Agubra, D. Flores, H. Campos, J. Villareal, M. Alcoutlabi, *J. Alloys Compd.* **2016**, *686*, 733.
- [27] R. O. Chavez, T. P. Lodge, J. Huitron, M. Chipara, M. Alcoutlabi, *J. Appl. Polym. Sci.* **2021**, *138*, 50396.
- [28] N. Obregon, V. Agubra, M. Pokhrel, H. Campos, D. Flores, D. De la Garza, Y. B. Mao, J. Macossay, M. Alcoutlabi, *Fibers* **2016**, *4*, 20.
- [29] V. A. Agubra, D. De la Garza, L. Gallegos, M. Alcoutlabi, *J. Appl. Polym. Sci.* **2016**, *133*, 42847.
- [30] B. Weng, F. Xu, M. Alcoutlabi, Y. Mao, K. Lozano, *Cellulose* **2015**, *22*, 1311.
- [31] D. De la Garza, F. De Santiago, L. Materon, M. Chipara, M. Alcoutlabi, *J. Appl. Polym. Sci.* **2019**, *136*, 47480.
- [32] A. M. Zepeda, D. Gonzalez, L. G. Heredia, K. Marquez, C. Perez, E. Pena, K. Flores, C. Valdes, T. M. Eubanks, J. G. Parsons, J. Cantu, *Microchem. J.* **2018**, *141*, 188.
- [33] A. Koski, K. Yim, S. Shivkumar, *Mater. Lett.* **2004**, *58*, 493.
- [34] S. Koombhongse, W. Liu, D. H. Reneker, *J. Polym. Sci., Part B: Polym. Phys.* **2001**, *39*, 2598.
- [35] A. Yang, X. Tao, G. Kin, H. Pang, K. Guei, G. Siu, *J. Am. Ceram. Soc.* **2008**, *91*, 257.
- [36] M. E. Mackay, A. Tuteja, P. M. Duxbury, C. J. Hawker, B. Van Horn, Z. B. Guan, G. H. Chen, R. S. Krishnan, *Science* **2006**, *311*, 1740.
- [37] N. Jouault, D. Zhao, S. K. Kumar, *Macromolecules* **2014**, *47*, 5246.
- [38] N. R. Tanguy, J. N'Diaye, M. Arjmand, K. Lian, N. Yan, *Chem. Commun.* **2020**, *56*, 1373.
- [39] N. Wan, X. Lu, Y. Wang, W. Zhang, Y. Bai, Y.-S. Hu, S. Dai, *Sci. Rep.* **2016**, *6*, 1.
- [40] R. Subasri, T. Shinohara, *Electrochem. Commun.* **2003**, *5*, 897.
- [41] D. Toloman, O. Pana, M. Stefan, A. Popa, C. Leostean, S. Macavei, D. Silipas, I. Perhaita, M. D. Lazar, L. Barbu-Tudoran, *J. Colloid Interface Sci.* **2019**, *542*, 296.
- [42] J.-M. Wu, H. C. Shih, W.-T. Wu, *Nanotechnology* **2005**, *17*, 105.
- [43] C. Su, B.-Y. Hong, C.-M. Tseng, *Catal. Today* **2004**, *96*, 119.
- [44] Q. Liu, L. Wang, K. Zhao, W. Yan, M. Liu, D. Wei, L. Xi, J. Zhang, *Electrochim. Acta* **2020**, *354*, 136727.
- [45] W. Wang, Y. Li, L. Li, L. Wang, K. Wang, *Int. J. Electrochem. Sci.* **2020**, *15*, 11709.
- [46] R. Li, W. Xiao, C. Miao, R. Fang, Z. Wang, M. Zhang, *Ceram. Int.* **2019**, *45*, 13530.
- [47] B. S. Lee, *Polymer* **2020**, *12*, 2035.
- [48] F. Liberale, M. Fiore, R. Ruffo, R. Bernasconi, S. Shiratori, L. Magagnin, *Sci. Rep.* **2020**, *10*, 13233.
- [49] L. W. Ji, P. Meduri, V. Agubra, X. C. Xiao, M. Alcoutlabi, *Adv. Energy Mater.* **2016**, *6*, 1502159.
- [50] X. L. Li, Y. L. Zhang, T. T. Li, Q. N. Zhong, H. Y. Li, J. M. Huang, *Electrochim. Acta* **2014**, *147*, 40.

## SUPPORTING INFORMATION

Additional supporting information may be found in the online version of the article at the publisher's website.

**How to cite this article:** G. Gonzalez, M. T. Hasan, D. Ramirez, J. Parsons, M. Alcoutlabi, *Polym. Eng. Sci.* **2022**, *62*(2), 360. <https://doi.org/10.1002/pen.25799>